W.A. Houlberg, S.E. Attenberger, L.R. Baylor, M. Gadeberg, T.C. Jernigan, P. Kupschus, S.L. Milora, G.L. Schmidt, D.W. Swain, M.L. Watkins and JET Team

Pellet Penetration Experiments on JET

Pellet Penetration Experiments
on JET

W.A. Houlberg[1], S.E. Attenberger[1], L.R. Baylor[1], M. Gadeberg, T.C. Jernigan[1],
P. Kupschus, S.L. Milora[1], G.L. Schmidt[2], D.W. Swain[1], M.L. Watkins
and JET Team*

JET-Joint Undertaking, Culham Science Centre, OX14 3DB, Abingdon, UK

[1]*Oak Ridge National Laboratory, Oak Ridge, Tennessee, USA*
[2]*Princeton Plasma Physics Laboratory, Princeton, New Jersey, USA*
* See Annex

PELLET PENETRATION EXPERIMENTS ON JET

W.A. HOULBERG*, S.E. ATTENBERGER*, L.R. BAYLOR*,
M. GADEBERG, T.C. JERNIGAN*, P. KUPSCHUS,
S.L. MILORA*, G.L. SCHMIDT**, D.W. SWAIN*,
M.L. WATKINS
JET Joint Undertaking,
Abingdon, Oxfordshire,
United Kingdom

ABSTRACT. The measured penetration depth, λ, of deuterium pellets injected into the Joint European Torus (JET) confirms some features of the neutral gas shielding (NGS) model, but not others. The scaling of λ with plasma and pellet parameters agrees with the NGS model, as in earlier ASDEX studies. Pellet velocity was varied over the range 0.46–1.35 km/s in the JET experiments to test specifically the scaling of λ with velocity. This scaling also agrees with the NGS model. However, the penetration is deeper in JET than in ASDEX when corrected for expected machine size dependence. Furthermore, the measured penetration depths are greater (by nearly a factor of two) in JET than those predicted by local ablation calculations using the neutral gas shielding model with an incident Maxwellian distribution of electrons. Plasma shielding used in previous modeling of the JET penetration data can account for the additional shielding but also removes the observed velocity dependence. The implications of both the scaling observations and the penetration depths for improvements in ablation theory and models are discussed.

1. INTRODUCTION

Fueling magnetically confined plasmas by injection of frozen hydrogenic pellets offers flexibility in the control of plasma density that is not attainable with fueling by neutral gas injection and recycle alone. The bulk of the pellet mass is ablated and ionized in the core, as demonstrated in many experiments over more than a decade [1–11]. Improved core

---

Permanent addresses:

*Oak Ridge National Laboratory, Oak Ridge, Tennessee, USA

**Princeton Plasma Physics Laboratory, Princeton, New Jersey, USA

fueling is a particularly important issue for future tritium experiments and is expected to correlate with pellet penetration depth, as well as to produce more peaked density profiles and higher fusion reaction rates. Additional benefits of direct core fueling by pellets have been the driving force in experiments thus far: higher plasma densities can be attained before reaching a disruption limit, and improved energy confinement is also frequently observed. These benefits provide the basic motivation for a better understanding of the ablation process and its dependence on both pellet and plasma parameters.

We reproduce in Section 2, in a modified form, the derivation of the scaling law for pellet penetration first derived by Parks [12] for the neutral gas shielding (NGS) model, as well as a derivation of the scaling law for plasma shielding [13]. The primary difference between them is in the lack of velocity dependence in the plasma shielding model, deriving from the (empirical) choice of the flux tube radius. Pellet size and velocity are the two primary pellet parameters possibly governing penetration depth, λ. Since pellet size is restricted by the maximum perturbation that can result from each pellet, velocity is a critical parameter for increasing penetration depth.

The pellet injector and diagnostic systems of the Joint European Torus (JET) are summarized in Section 3. We present in Section 4 some of the first experimental data on the velocity dependence of pellet penetration in JET. These data confirm the NGS scaling law for λ, in agreement with earlier ASDEX analyses [8,14], but raise questions about the magnitude of the penetration depth. The penetration is deeper in JET than in ASDEX when corrected for the expected dependence on machine size. The reduced penetration in ASDEX has the appearance of an edge effect that is only partially explained by a pedestal in the edge temperature [8].

In Section 5 we calculate λ from local ablation models using the PELLET code [15] with several variations of the NGS model and compare the calculated values with the experimental results. The simplest form of the NGS model with monoenergetic plasma electrons reproduces the data remarkably well, but the NGS model with Maxwellian plasma electrons leads to enhanced ablation and values of λ much lower than the JET data. The empirical addition of plasma shielding can be used to bring the magnitude of the calculated λ's into agreement with the experimental results, as we showed in earlier work [13,16], but also removes the velocity scaling. Another mechanism is needed to enhance the effective shielding in the cloud by the factor of 15 needed to bring the NGS model with Maxwellian

electrons into agreement with the JET data. We speculate on several possible mechanisms, including cold plasma shielding, ellipticity of the neutral gas cloud, magnetic shielding, and electrostatic effects, noting also the apparent discrepancy between JET and ASDEX results.

2. PENETRATION SCALING

The steady-state solution to the hydrodynamic equations for a spherically expanding neutral gas cloud is governed by the source of neutral gas at the pellet surface (pellet erosion rate) and by the heating of the neutral gas cloud by plasma electrons incident on the cloud. The source of neutral gas at the pellet surface is in turn determined by the heat flux at the pellet surface, attenuated by the neutral gas (self-shielding factor). A simplified relationship between the pellet surface erosion rate $\dot{r}_p$, the effective spherical pellet radius r_p, the molecular density of solid hydrogen n_m, the atomic mass number of the ablatant A_p, and the background plasma electron density n_e and temperature T_e is given approximately by [12,17]

$$\dot{r}_p \equiv \frac{dr_p}{dt} \propto \frac{n_e^{1/3} T_e^{5/3}}{A_p^{1/3} n_m r_p^{2/3}} \tag{1}$$

where $n_m = 2.12 \times 10^{28} + 6.30 \times 10^{27} A_p - 8.66 \times 10^{26} A_p^2$ m^{-3}. For simplicity of integration, we assume that the plasma electron density and temperature profiles can be expressed as $n_e(x) = n_{e0}(1-x)^{\alpha_n}$ and $T_e(x) = T_{e0}(1-x)^{\alpha_T}$, respectively, where n_{e0} and T_{e0} designate values at the minor axis of the plasma (magnetic axis), $x = r/a_0$ is a dimensionless measure of the plasma minor radius, and a_0 is the distance from the magnetic axis to the outer plasma edge in the midplane. Time can be removed by relating it to the location of the pellet in the plasma assuming constant pellet velocity: $dt = -a_0 dx/v_p$, where v_p is the pellet velocity (injection normal to the plasma from the outside midplane, typical of most experiments). Note that the only way pellet velocity and characteristic machine size enter the derivation of the penetration depth is through the conversion of dt to dx. Integrating over the life of the pellet (dr from an initial radius of r_{p0} to 0, and dx from pellet entry at $x = 1$ to $1 - \lambda/a_0$, where λ is the final penetration depth) gives

$$\frac{\lambda}{a_0} \propto \left(\frac{v_p n_m A_p^{1/3} r_{p0}^{5/3}}{a_0 n_{e0}^{1/3} T_{e0}^{5/3}} \right)^{\beta_{ngs}} = (C_p v_p)^{\beta_{ngs}} \tag{2}$$

where $\beta_{ngs} \equiv 3/(3 + \alpha_n + 5\alpha_T)$. We define the lumped parameter in parentheses as $C_p v_p$ and note that for linear profiles ($\alpha_n = \alpha_T = 1$) $\beta_{ngs} = 1/3$, as noted by Parks [12]. Injection

3

from other than the outside midplane normal to the plasma minor axis modifies the choice of characteristic dimension a_0 and the relationship between pellet position and plasma parameters, and is easily accommodated in more detailed pellet ablation models.

In analysis of ASDEX results, Büchl et al. [8] restricted their analysis to $\alpha_n = \alpha_T = 1$ and allowed for an edge pedestal on $T_e(x)$ for better representation of the profiles for shallow penetration. Büchl et al. defined the scaling parameter

$$Z \equiv \frac{d_p^{5/3}(\text{mm})v_p(\text{km/s})}{n_{e0}^{1/3}(10^{13}\ \text{cm}^{-3})T_{e0}^{5/3}(\text{keV})} \tag{3}$$

where d_p is the pellet diameter. Z is simply related to our choice of $C_p v_p$ in mks-keV units by $Z = 1.79 \times 10^{-21} a_0 C_p v_p$. Since both JET and ASDEX use deuterium pellets, the only substantial difference in the scaling expressions is the introduction of a_0 in $C_p v_p$. An edge pedestal introduces an offset in the penetration depth. For typical Ohmic and H-mode profiles in ASDEX the expected penetration depths calculated from Parks's NGS model [12] are given by Büchl et al. as

$$\frac{\lambda_{\text{OH}}}{a_0} = 0.858 Z^{1/3} - 0.085 \tag{4}$$

$$\frac{\lambda_{\text{NBI}}}{a_0} = 0.905 Z^{1/3} - 0.176 \tag{5}$$

respectively, where $a_0 = 0.40$ m has been used to normalize the penetration depth.

The use of a Maxwellian distribution of electrons from the background plasma yields a higher ablation rate than a monoenergetic model with electrons at $3T_e/2$ because of the $1/E$ dependence of the electron stopping cross-section above 1 keV [15]. A simple extension of the NGS model with Maxwellian electrons then gives much lower pellet penetration than observed experimentally (as we discuss further in Section 5). Additional shielding is necessary, and this can be provided by the ionized ablatant trapped in a flux tube connected to the pellet [15,16]. We called this the neutral gas and plasma shielding (NGPS) model, the most notable feature of which is its lack of dependence on the pellet velocity [13]. To distinguish between the NGS and NGPS models was a motivation for the explicit variation of velocity in the JET experiments.

The scaling of penetration depth for the NGPS model when plasma shielding dominates can be derived from the stopping cross-section for energetic electrons in a cold plasma, the source strength, and the ionizing or confinement radius defining the cold plasma tube [13]. The line-integrated cold plasma density (integration along the axis of a flux tube connected

to the pellet) required to stop electrons of energy $E_e \propto T_e$ is given by $\int n_c dl \propto T_e^2$. The total number of cold ions in the tube is given by $A_c \int n_c dl$, where $A_c \equiv 2\pi r_c^2$ is the cross-sectional area of a tube of radius r_c. The total number of cold ions in the tube is also given by the product of the source rate at the pellet surface $\dot{N} \equiv n_m 4\pi r_p^2 \dot{r}_p$ and the time the pellet takes to traverse a distance corresponding to the diameter of the tube $t_p = 2r_c/v_p$. The expression for the pellet surface recession rate is then

$$\frac{dr_p}{dt} \propto \frac{v_p r_c T_e^2}{n_m r_p^2} \tag{6}$$

The relationship between time and position for a constant velocity pellet then removes any velocity dependence from Eq. (6). When $r_c \propto r_p$, and the equation is integrated for electron density and temperature profiles as assumed for the NGS model, the scaling model for penetration depth becomes

$$\frac{\lambda}{a_0} \propto \left(\frac{n_m r_{p0}^2}{a_0 T_{e0}^2} \right)^{\beta_{p_s}} \tag{7}$$

where $\beta_{p_s} \equiv 1/(1 + 2\alpha_T)$. For a linear temperature profile, the scaling with pellet size and electron temperature is very close to that given by the NGS model. The only way velocity scaling can be reintroduced in the plasma shielding model is through a velocity dependence of the effective confinement radius, $r_c = r_c(v_p)$.

3. EXPERIMENTAL ARRANGEMENT

The multiple-pellet injector on JET was developed at ORNL and consists of three single-stage light gas guns, each capable of independently firing multiple pellets and each with its own diagnostic system [18,19]. The pellets are nominally cylinders of equal length and diameter of 2.7 mm, 4.0 mm, and 6.0 mm for the three guns.

Several diagnostics are used to measure pellet parameters for each of the three guns. A video monitor of the D_2 extrusion is used to check the quality of the D_2 ice. Pellet mass, velocity, and penetration depth are determined from the signals generated by a fiber-optic pellet interrupter triggering system, a double microwave cavity bridge, and a photodiode for measuring pellet line emission (primarily D_α) during pellet ablation. These are passed through a summing amplifier and illustrated in Fig. 1 for a slow 2.7 mm pellet and in Fig. 2 for a typical 4.0 mm pellet. A timing signal corresponding to the approximate time when the pellet crosses the reference outer limiter position of $R_{\text{lim}} = 4.132$ m is generated electronically from the pellet speed as measured between the photodiode and first microwave

5

signals (see Figs 1 and 2). A more accurate time for this signal, also shown in Figs 1 and 2, is calculated from the velocity determined by the two microwave signals during postprocessing.

The double microwave cavity bridge provides a direct measure of the relative pellet mass [19]. At nominal operating conditions the relationship between the output voltage and pellet mass for the three guns is given by $V_{2.7} \propto M^{2.2}$, $V_{4.0} \propto M^{1.4}$, and $V_{6.0} \propto M^{0.78}$. Figures 1(b) and 2(b) show expanded scales for the microwave signals for a 2.7 mm and a 4.0 mm pellet, respectively. The masses as determined from the microwave signals agree with the Δn_e produced in the plasma by 4.0 mm pellets, although the error bars in the density measurements precluded using this as a very accurate absolute calibration. We estimate error bars on the absolute calibration of the mass detectors at $\pm 15\%$. The relative error within the data on each gun is much smaller.

The speed can be determined from any two of the three signals from the fiber-optic interrupter trigger and the two microwave bridges (see Figs 1(b) and 2(b)). We found that the fiber-optic signal was triggering early for the low velocity pellets — apparently from propellant gas blow-off preceding the pellet by up to 0.02 m — so the timing between the microwave peaks was used to determine velocity. The distance between the photodiode and the center of the first microwave cavity is $D_{p-\mu 1} = 0.593$ m, and that between the centers of the two cavities is $D_{\mu 1 - \mu 2} = 0.416$ m. The maximum systematic error in the velocity determined from timing between the photodiode and first microwave signals reached as high as 3.5%, which produced highly inaccurate penetration depths. When the centers of the microwave peaks are determined from a least-squares fit to a Gaussian, the error in the velocity is estimated to be $\pm 0.3\%$.

The penetration depth in the plasma is determined by two means: (1) time of flight using the pellet velocity and the time interval between the second microwave signal and the end of the D_α signal, and (2) an absolute measurement from a vertical soft X-ray (SXR) detector array located above the pellet injection line. Both methods introduce potential errors, which have been carefully examined.

The accuracy of the time-of-flight measurement is limited by the accuracy of the velocity measurement, the accuracy of determining the end of the D_α signal, and the assumption of constant velocity and straight trajectory during the entire free-flight and ablation time. The distance between the second microwave signal and the magnetic axis (≈ 7.5 m) is much greater than $D_{\mu 1 - \mu 2}$, so very high accuracy is required in determining the velocity.

The error, δR_{v_p}, in the penetration depth of a pellet approaching the magnetic axis is $\delta R_{v_p} \approx 7.5(\delta v_p / v_p)$ m, giving ± 0.022 m with v_p determined from the microwave signals. The error in penetration associated with the error in determining the end of the D_α signal is $\delta R_{D_\alpha} = v_p \delta t_{D_\alpha}$. The end of the D_α signal for the low velocity 2.7 mm pellets is often difficult to determine as accurately as that shown in Fig. 1(c), while the traces from the larger 4.0 mm and 6.0 mm pellets are typically as sharply defined as the example in Fig. 2(c). An upper limit of $\delta t_{D_\alpha} = \pm 60 \,\mu s$ for 2.7 mm pellets and $\pm 30 \,\mu s$ for the larger pellets leads to $\delta R_{D_\alpha} = \pm 0.08$ m and ± 0.04 m, respectively. Overall, we assign error estimates of ± 0.10 m for the 2.7 mm pellets and ± 0.05 m for the larger pellets.

The only means of testing the constant v_p assumption in JET is to examine the vertical SXR signals or to compare the penetration depth with that from the SXR analysis. We have found no clear evidence in JET data of any significant change in the velocity component tangent to the initial pellet direction.

The horizontal and vertical SXR detector arrays located adjacent to and above the pellet injection line provide a second means of determining the pellet penetration depth. Each channel of the vertical SXR detector views a zone of width 0.06–0.07 m in major radius at the midplane. The toroidal view of ± 0.3 m is wide enough so that pellets should not curve out of view. A 5 ms window, digitized at 200 kHz around the time the pellet enters the torus, provides high time resolution. Pellet penetration is determined from a contour plot of detector array data (time and major radius in the midplane of vertical detector view) as shown in Figs 3 and 4 for 2.7 mm and 4.0 mm pellets, respectively. The time for termination of the enhanced signal from the pellet is taken from one of the horizontal channels. The intersection of a line drawn through the peaks of the intensities with the termination time of the horizontal signal yields the penetration depth. The slope of the line through the peaks can be used to check pellet velocity, but the accuracy is far less than the velocity determined from the microwave bridge signals. The random error in determining the end point of the SXR signals is estimated to be ± 0.03 m for the high velocity pellets and ± 0.05 m for the lower velocity pellets. The amplitude of the signal is smaller for the low velocity pellets and its termination less certain, as can be seen by comparing Figs 3 and 4. Correction of a systematic error of 0.065 m ($R = R_s + 0.065$ m) is required to account for recalibration of the detector location (0.02 m outward) and tilt under discharge conditions (0.7 degrees, or 0.045 m outward) with a random error in this correction of ± 0.03 m. Overall, we estimate

error bars of ±0.10 m for the 2.7 mm pellets and ±0.05 m for the larger pellets. There is excellent agreement between the SXR and time-of-flight penetration determinations, as shown in Fig. 5.

Plasma parameters for the pellet injection experiments were obtained from the standard set of JET diagnostics, including the six channel far-infrared (FIR) interferometer data for electron density profiles and second harmonic electron cyclotron emission (ECE) data for electron temperature profiles. The FIR-inverted density profiles have been compared with the 0.5 Hz LIDAR density profiles [20,21] for many pellet cases and the agreement is good. Since pellet ablation is not very sensitive to the density or the shape of the density profile, high accuracy is not critical; the uncertainty in the density profile for these experiments is estimated to be ±10%. The ECE temperature profile measurement has an absolute accuracy of ±10% and a relative accuracy between spatial points of ±5%.

In the pellet velocity experiments on JET the injector was tuned to vary the pellet speed from 0.46 to 1.35 km/s. This tuning was accomplished by adjusting the duration of the propellant valve opening time. The slower pellet velocities were achieved with a valve opening time of 0.9–1.0 ms, while the higher velocity pellets required an opening time of 1.5–1.6 ms. The propellant (hydrogen) pressure in the injector was maintained at 62 bar (900 psia) during these experiments. Keeping the propellant pressure constant while varying the valve opening time simplified the procedures for varying pellet velocity on a shot-by-shot basis, with the low velocity pellets being reasonably reproducible.

4. EXPERIMENTAL RESULTS

The experimental results from several hundred pellets injected during the 1989 run were examined. Essentially all of the data were generated in a parasitic mode of operation in which pellets were injected either to augment experimental investigations focussed on another topic or in the very early or late stages of a discharge before or after the primary program. These pellets were therefore subjected to a wide variety of discharge conditions, and no attempt was made to preselect the data based on target parameters, except in the low velocity experiments. In those cases, high and low velocity pellets were injected at the same time points in nearly identical sequential plasmas to eliminate as many uncertainties as possible in the evaluation of velocity scaling. Pellet mass integrity (no indication of a broken pellet from the microwave cavity signals), velocity, penetration depth from either

8

the time-of-flight or SXR analyses, T_e either in flat-top or measured very shortly before pellet injection, and n_e with no indication of lost FIR interferometer fringes were critical for accepting a pellet into the penetration database.

Figure 6 summarizes the range of parameters for 96 cases that survived these acceptance criteria, with circles (o) denoting the 64 cases that also survived the following two additional criteria and crosses (×) denoting those that did not survive these criteria: (1) penetration to less than 90% of the distance to the magnetic axis and (2) mass indication from the microwave signal greater than 25% of the nominal mass to ensure reliability of the signal calibration. Penetration to near or beyond the axis invalidates the use of preinjection plasma parameters in the scaling studies; strong self-limiting ablation effects near the axis and ablation beyond the axis both require corrections to the ambient plasma conditions. Unfortunately, all but one of the 6 mm pellets failed to meet this criterion, and the one surviving case was very near the imposed penetration limit. Later, we discuss tentative results from analysis of four 6 mm data points from the 1990 run that are not included in this database because of lack of microwave cavity signals. Estimates for mass and velocity are used for preliminary analysis of penetration for these large pellets. The mass criterion eliminated a few of the 4 mm pellets. The axial electron temperature spans 1.0–4.58 keV for those pellets meeting all acceptance criteria (o's in Fig. 6(a)), and the axial density 0.13–1.00 $\times 10^{20}$ m^{-3} (Fig. 6(b)), with the higher temperatures occurring during ion cyclotron range of frequencies (ICRF) or neutral beam injection (NBI) heating and the higher densities usually from prior pellets in a multiple-pellet sequence. The masses of the 2.7 mm pellets averaged around 70% of the nominal mass but varied by nearly a factor of 3 at the extremes, while the 4 mm pellets were centered about the nominal mass with a few obvious partial pellets, and the 6 mm pellets varied from 80 to 100% of the nominal mass as seen in Fig. 6(c). The usual velocity ranges of 2.7 and 4 mm pellets vary from nominally 1.1 to 1.3 km/s, as shown in Fig. 6(d) (varying with the propellant pressure setting and depending on whether single or multiple pellets are injected), while the 6 mm pellets are all single-pellet sequences and tightly grouped at 1.3 km/s. Nine 2.7 mm pellets are grouped around 0.5 km/s for a specific test of velocity scaling.

The penetration depth for the experimental data is defined as the distance the pellet traveled beyond $R_{\text{lim}} = 4.132$ m (the position of the ICRF antenna guard limiters), giving $\lambda \equiv R_{\text{lim}} - R_{\text{pen}}$. λ is normalized to the distance between a nominal magnetic axis position at

9

3.00 m and the limiter, $a_0 = 1.132$ m. The actual position of the magnetic axis is dependent on discharge conditions (diverted plasma or inner or outer limiter, plasma current, beta, etc.). Sufficient and consistent magnetic analyses were not available just before each of the pellets to warrant a case-by-case normalization of the penetration depth. Normalization to a constant characteristic dimension in the following data then introduces some uncertainty when comparing the results to theoretical models for penetration depth.

Figure 7 shows the range of normalized penetration depths for each nominal pellet size, with the $\lambda/a_0 < 0.9$ cutoff also indicated. The 2.7 mm pellets rarely reached the axis; those that did were usually subsequent pellets in multiple-pellet sequences during the current ramp-up phase when axial electron temperatures were $T_{e0} \approx 1$ keV. The 4 mm pellets exhibited a mean penetration depth of $\lambda/a_0 \approx 0.9$ (the injection timing in auxiliary-heated plasmas was often chosen such that penetration would be nominally to the axis); all but one of the 6 mm pellets penetrated beyond $\lambda/a_0 = 0.9$.

In Fig. 8 the relationship between the normalized penetration depth and the parameters theoretically expected to influence penetration is examined. Some of the higher velocity pellets did not penetrate as far as the low velocity pellets (Fig. 8(a)) so correction for other plasma and pellet parameters is necessary. When λ/a_0 is plotted against the lumped parameter derived from the NGS model, C_p, it is seen that λ/a_0 contains a definite velocity dependence that separates the high and low velocity data (Fig. 8(b)). Plotting the penetration depth against the product $C_p v_p$ as in Fig. 8(c) brings all the data into line. The least-squares fit to the data shown in Fig. 8(c) is given by

$$\lambda/a_0 = 2.35 \times 10^{-9}(C_p v_p)^{0.426} \tag{8}$$

where parameters in $C_p v_p$ (Eq. (2)) are given in mks units and T_e is in keV. The four pairs of high and low velocity pellets injected into nearly identical plasmas were separately analyzed, and each case exhibited a velocity dependence in agreement with the fit of Eq. (8).

The exponent of the fit can be used to infer information about the density and temperature profiles, since $\beta = \beta_{\text{ngs}} \equiv 3/(3 + \alpha_n + 5\alpha_T)$. The sensitivity to the electron density profile is weak, so that if α_n spans the range from 0 to 1 (flat to linear profiles) then the fit implies that $\alpha_T = 0.6$–0.8. Typical normalized ECE electron temperature and FIR-inverted electron density profiles are shown in Fig. 9 along with the inferred fits. The assumed profile form, especially for T_e, is not a very good representation of the data and would lead to some deviations in the agreement between the actual and expected scalings of the penetration

10

depth. This difference becomes obvious when we compare penetration depths calculated from a local model with the empirical fit in Section 5.

As noted in Section 2, Büchl et al. allowed for a pedestal in T_e at the plasma edge in the analysis of ASDEX results [8]. In terms of the dimensionless penetration depth, the fit of Büchl et al. [8] to the ASDEX data is given by

$$\frac{\lambda}{a_0} = 0.875 Z^{1/3} - 0.263 \tag{9}$$

The offset is larger than expected for either Ohmic or H-mode profiles, as given in Eqs (4) and (5), and led Büchl et al. to conclude that ablation in the plasma periphery is higher than theoretically expected, but not readily explained by either fast beam ion or runaway electron effects. The normalized penetration in JET experiments is greater than that observed by Büchl et al. [8] in ASDEX experiments (Fig. 10). Without the offset, the empirical fit to the ASDEX data agrees reasonably well with the JET fit (Fig. 10).

The JET penetration data have been examined for their sensitivity to pellet mass and heating method. In Fig. 11 we plot the measured penetration depths against the empirical fit for each pellet type and sort the data by heating method. Data from four 6 mm pellets injected during the 1990 run are also illustrated. These are assigned values of mass (90% of nominal) and velocity (1.32 km/s) estimated from the 1989 data shown in Fig. 6 because the microwave signals were not available for the 1990 run. The propellant pressure and valve settings on the gun were unchanged from 1989, and since little scatter was observed in the data during previous operation, the additional errors introduced by these approximations are expected to be minimal. Auxiliary heating with either NBI or ICRF shows no obvious effect on penetration depth other than through the changes in T_e in these data. All of these cases represent relatively low auxiliary power densities (up to 7 MW) and do not necessarily contradict observations of enhanced ablation with strong auxiliary heating on other machines. The pellet mass variation spans more than an order of magnitude. Its effect on penetration is reasonably consistent with the expected scaling from the NGS model, although the absolute calibration for each of the pellet sizes is not very precise.

5. EVALUATION OF LOCAL ABLATION MODELS

The penetration depth was calculated for each of the 64 pellet cases of Section 4 using the PELLET code [15], with various adaptations of the NGS model. The normalized density

and temperature profiles shown in Fig. 9 were used for all cases and scaled to the measured central values in an attempt to simplify the analysis. Although some variation in the electron temperature profiles was noted, none of the cases had strong enough heating for $T_e(\rho)/T_e(a_0)$ to deviate significantly from that typical of Ohmic plasmas. The density profiles vary considerably, especially for subsequent pellets in a multiple-pellet sequence, but the weak dependence of ablation on plasma density reduces the effect of variations in the density profile. Two other sets of normalized profiles were also examined and gave results similar to those presented here. We compare only the penetration depth (corresponding to the end of the pellet life) with experimental values. We have not performed any systematic analysis of the correspondence between the calculated local ablation rate and either the shape of the D_α trace or the $\Delta n_e(\rho)$ profile, but find significant differences in the few cases that have been examined. This will be the subject of future work.

The NGS model with a monoenergetic electron distribution reproduces both the experimental data and the empirical scaling remarkably well (Fig. 12). The scatter in the comparison with experimental values, Fig. 12(a), is in part due to variation in the profiles from the reference case. When the calculated results are compared to the empirical fit, Fig. 12(b), the effect of the variation of the profiles from the assumed form is seen. The shallower penetrating pellets ($\lambda/a_0 < 0.5$) see a lower temperature on the average than that of the empirical form $(1 - x)^{\alpha_T}$, as seen in Fig. 9(b) (using the broad density profile result, $\alpha_n = 0$). More deeply penetrating pellets see a higher temperature (ablation is weighted toward the end of the pellet life). The calculated penetration depth of the 6.0 mm pellet includes a strong self-limiting ablation effect as the pellet approaches the magnetic axis that is not adequately reproduced by the empirical fit.

The stopping cross-section for an electron of energy E_e in a gas decreases as $1/E_e^2$ for $E_e > 1$ keV. If we require more than 99.9% of the incident energy flux to be attenuated before reaching the pellet surface, the shielding must be much larger for a Maxwellian distribution of incident particles than for a monoenergetic distribution at the mean energy [15]. When a Maxwellian electron distribution of incident electrons is used in the NGS model, the ablation is enhanced to support the extra shielding, and the calculated penetration is well below the experimental observations, as seen in Fig. 13. The lower penetration data are not as strongly affected by the Maxwellian approximation since the temperature over much of the pellet lifetime is below 1 keV where the stopping cross-section is a weaker function of

energy.

A straightforward way to bring the NGS model with Maxwellian electrons into agreement with experimental results is to add a shielding enhancement factor, f_E, as an amplification of the stopping in the neutral gas cloud. $f_E = 15$ reproduces the JET data very well (Fig. 14). Strong enhancement of the shielding is required because f_E enters $C_p v_p$ as $f_E^{1/3}$, giving $\lambda/a_0 \propto f_E^{1/9}$ in the linear profile approximation, $\alpha_n = \alpha_T = 1$. This leaves open the question of the source of the extra shielding.

When plasma shielding is added as in the NGPS model with the plasma tube radius given by $r_c = r_p + 1$ mm [13,16], the calculated penetration of the higher velocity pellets agrees with experimental observations (Fig. 15) within the experimental error bars on the measured penetration (see Figs 8 and 11). However, the calculated penetration of low velocity pellets is consistently much deeper than observed, reflecting the domination of the plasma shielding contribution (more than 90%) and its lack of velocity dependence. Examination of Eq. (5) suggests that we would need $r_c \propto r_p/v_p$ to reintroduce the observed scaling with pellet velocity. This may be possible if a portion of the ionized ablatant is dragged along with the pellet [22].

What other shielding mechanisms can be so large and yet preserve the basic NGS scaling? Ellipticity of the neutral cloud, magnetic shielding, and electrostatic effects are potential candidates. Ellipticity may contribute to f_E [23], but a factor of 15 may be too high for this to be the sole contribution. Magnetic shielding is unlikely to contribute more than a factor of 2 [22,24,25]. The effect of the ambipolar potential has recently been revisited by Rozhanskii [26]. He found a potential drop of $e\phi \approx 2kT_e$ between the hot plasma and the cold ablatant plasma. This attenuates the electron heat flux incident on the cold ablatant by $\exp(-e\phi/kT_e)$, leaving an anomaly of only 2 in the shielding factor in the JET data. Since this effect scales with the electron temperature, it preserves the NGS scaling.

6. DISCUSSION

Pellet penetration in JET confirms some features of the NGS model, including the velocity dependence, and in this regard confirms earlier ASDEX observations. The depth of penetration raises some questions, however.

There are several possibilities for the source of the difference in penetration between JET and ASDEX that require further evaluation. The ASDEX axial density and temper-

ature ranges, as well as pellet velocities, overlap the JET data, and both use D_2 pellets. Plasma size and pellet velocity can enter only through the conversion of time in the combination v_p/a_0 in the NGS model. Since the results confirm the velocity scaling, it is difficult to imagine how plasma size scaling could differ from the assumed form. Possible hidden dependences on plasma (e.g. magnetic field, energetic particles, profile shape) and pellet (e.g. shape, integrity) parameters are the only remaining differences. A pedestal in T_e at the plasma edge, pellet size, and magnetic field strength are the most likely sources of the difference.

Pellet size is the only parameter for which JET and ASDEX data do not overlap. The nominal mass of the smallest JET pellets is four times the nominal mass of the largest ASDEX pellets. The scaling of λ with mass may be stronger than the model predicts but masked in the JET data by the uncertainty in the absolute calibration of the masses for each injector. In a statistical analysis of the ASDEX data, Loch et al. [14] noted a slightly higher mass dependence than the NGS model predicts: $\lambda \propto M_p^{0.26}$ for Ohmic discharges and $M_p^{0.28}$ for NBI heating versus $M_p^{0.19}$ for $\beta = 1/3$. This discrepancy is not large enough to explain the difference between the JET and ASDEX results. An effect neglected in the NGS model is the mass lost in establishing the initial neutral gas shield; the NGS model assumes a steady-state solution to the hydrodynamic expansion of the cloud at all times. For the smaller ASDEX pellets, this approximation may begin to break down.

Essentially all the JET pellet data have been generated at 3 T, while ASDEX typically operates at 2.2 T. The possible dependence of λ on B_T has not been examined in either device. B_T does not enter the NGS model in its original formulations, but it may affect the ionized portion of the ablatant, causing distortion of the magnetic field in the vicinity of the pellet (with a corresponding reduction of the heat flux incident on the cloud). The dependence of this distortion on magnetic field intensity is expected to be weak [22,24,25]. Net ablation would have to decrease strongly with magnetic field strength in order to bring the JET and ASDEX results into agreement. Because of the higher magnetic fields in the International Thermonuclear Experimental Reactor (ITER) [27] and ignition experiments such as the high field Burning Plasma Experiment (BPX) [28], this issue should be examined more closely.

Why does the original NGS model do such a remarkable job of predicting both the scaling and magnitude of pellet penetration in JET, when relaxation of some of the simplifying

14

assumptions can have such a dramatic impact on the results? The incorporation of a Maxwellian distribution of electrons is a relatively straightforward procedure. However, it reduces predicted penetration depths by nearly a factor of 2 from the monoenergetic model when $T_e > 1$ keV and requires a large increase in the shielding to compensate. A number of additional shielding effects have been examined in theoretical models — pedestals in the edge electron temperature [8], plasma shielding [15], ellipticity of the neutral gas shield [23], magnetic shielding [22,24,25], and electrostatic potential [26] — and each can potentially make significant contributions to the shielding under different pellet and plasma operating conditions. The essentially complete cancellation of two strong effects in the original NGS model — increased ablation from the use of a Maxwellian electron distribution and enhanced shielding — then has the appearance of being fortuitous.

Comparing data from different machines, as we have done for JET and ASDEX results, highlights differences that would otherwise go unnoticed, but as yet no firm conclusions may be drawn. Understanding the ablation process is important for the evaluation of pellet penetration capabilities in future devices such as ITER, which require the high fueling efficiency afforded by deeper pellet penetration. The JET penetration data explicitly confirm the NGS model predictions of increasing penetration with increasing velocity. However, greater confidence in the contributing ablation and shielding physics is needed for reliable extrapolation to larger pellets in hotter plasmas.

ACKNOWLEDGEMENTS

REFERENCES

[1] MILORA, S. L., FOSTER, C. A., THOMAS, C. E., et al., Nucl. Fusion **20** (1980) 1491.

[2] MILORA, S. L., SCHMIDT, G. L., HOULBERG, W. A., et al., Nucl. Fusion **22** (1982) 1263.

[3] GREENWALD, M., GWINN, D., MILORA, S., et al., in Plasma Physics and Controlled Nuclear Fusion Research 1984 (Proc. 10th Int. Conf. London, 1984), Vol. 1, IAEA, Vienna (1985) 45.

[4] SENGOKU, S., NAGAMI, M., ABE, M., et al., Nucl. Fusion **25** (1985) 1475.

[5] ANDREEV, A. P., KUTEEV, B. V., LOVTSYUS, A. A., SKOBLIKOV, S. V., UMOV, A. P., Sov. J. Plasma Phys. **12** (1986) 313.

[6] TFR GROUP, Europhys. Lett. **2** (1986) 267.

[7] HEIDBRINK, W. W., MILORA, S. L., SCHMIDT, G. L., SCHNEIDER, W., RAMSEY, A., Nucl. Fusion **27** (1987) 3.

[8] BÜCHL, K., VLASES, G. C., SANDMANN, W., LANG, R., Nucl. Fusion **27** (1987) 1939.

[9] SUDO, S., MOTOJIMA, O., SANO, F., et al., Nucl. Fusion **27** (1987) 1401.

[10] WURDEN, G. A., WEBER, P. G., WATT, R. G., et al., Nucl. Fusion **27** (1987) 857.

[11] SCHMIDT, G. L., JET TEAM, in Plasma Physics and Controlled Nuclear Fusion Research 1988 (Proc. 12th Int. Conf. Nice, 1988), Vol. 1, IAEA, Vienna (1989) 215.

[12] PARKS, P. B., TURNBULL, R. J., Phys. Fluids **21** (1978) 1735.

[13] HOULBERG, W. A., MILORA, S. L., BAYLOR, L. R., WATKINS, M. L., JET/USDOE PELLET COLLABORATION, in Pellet Injection and Toroidal Confinement (Proc. Tech. Committee Meeting, Gut Ising, 1988), IAEA-TECDOC-534, IAEA, Vienna (1989) 217.

[14] LOCH, R., SANDMANN, W., BÜCHL, K., LANG, R., MERTENS, V., in Controlled Fusion and Plasma Physics (Proc. 17th Eur. Conf. Amsterdam, 1990), Vol. 14B, Part I, European Physical Society (1990) 235.

[15] HOULBERG, W. A., MILORA, S. L., ATTENBERGER, S. E., Nucl. Fusion 28 (1988) 595.

[16] WATKINS, M. L., HOULBERG, W. A., CHEETHAM, A. D., et al., in Controlled Fusion and Plasma Physics (Proc. 14th Eur. Conf. Madrid, 1987), Vol. 11D, Part I, European Physical Society (1987) 201.

[17] MILORA, S. L., FOSTER, C. A., IEEE Trans. Plasma Sci. PS-6 (1978) 578.

[18] MILORA, S. L., COMBS, S. K., BAYLOR, L. R., FOUST, C. R., GETHERS, F. E., SPARKS, D. O., in Proc. 12th IEEE Symposium on Fusion Engineering (Monterey, 1987), Vol. 2, IEEE, New York (1987) 784.

[19] BAILEY, W., KUPSCHUS, P., GADEBERG, M., et al., in Fusion Technology (Proc. 15th Symp. Utrecht, 1988), Vol. 1, North Holland, Amsterdam (1989) 720.

[20] BARTLETT, D. V., CAMPBELL, D. J., COSTLEY, A. E., et al., in Controlled Fusion and Plasma Physics (Proc. 15th Eur. Conf. Dubrovnik, 1988), Vol. 12B, Part III, European Physical Society (1988) 1119.

[21] BAYLOR, L. R., HOULBERG, W. A., MILORA, S. L., SCHMIDT, G. L., KUPSCHUS, P., JET PELLET COLLABORATION TEAM, Nucl. Fusion 31 (1991) 1249.

[22] PARKS, P. B., Nucl. Fusion 31 (1991) 1431.

[23] KUTEEV, B. V., UMOV, A. P., TSENDIN, L. D., Sov. J. Plasma Phys. 11 (1985) 236.

[24] PARKS, P. B., Nucl. Fusion 20 (1980) 311.

[25] LENGYEL, L. L., Nucl. Fusion 29 (1989) 37.

[26] ROZHANSKII, V. A., Sov. J. Plasma Phys. 15 (1989) 638.

[27] TOSCHI, R., in Plasma Physics and Controlled Nuclear Fusion Research 1990 (Proc. 13th Int. Conf. Washington, D.C., 1990), Vol. 3, IAEA, Vienna (1991) in press.

[28] SIGMAR, D. J., BATCHELOR, D. B., BATEMAN, G., et al., in Plasma Physics and Controlled Nuclear Fusion Research 1990 (Proc. 13th Int. Conf. Washington, D.C., 1990), Vol. 3, IAEA, Vienna (1991) in press.
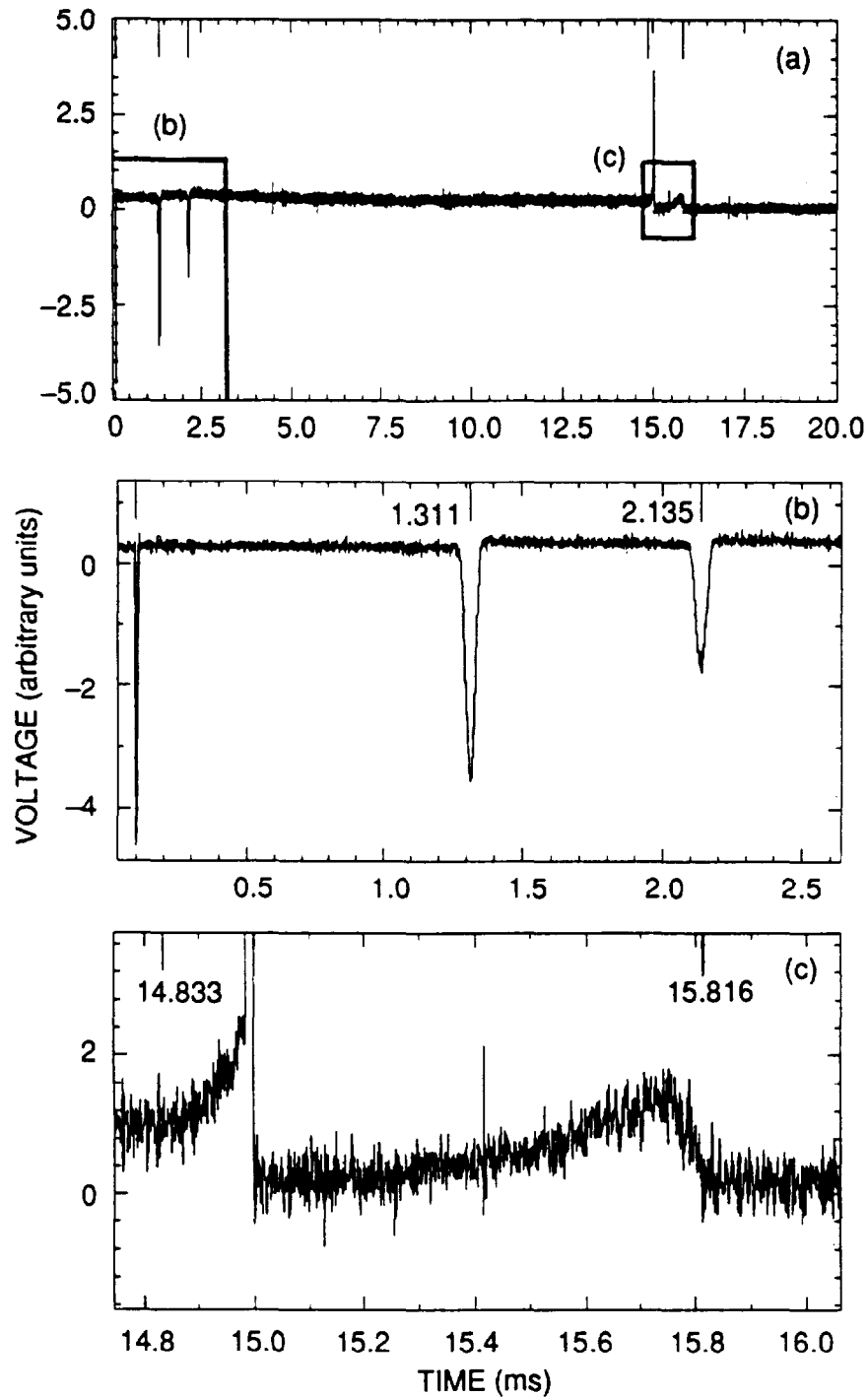
FIG. 1. Typical diagnostic trace (shot 20732, pellet 2) for determining the velocity, mass, and penetration depth of low velocity 2.7 mm pellets: (a) combined light diode, microwave cavity, timing, and D_α signals with times marked on the upper horizontal axis corresponding to initiation of the light diode signal, centers of the two microwave signals, expected arrival at $R_{lim} = 4.132$ m, and the end of the enhanced D_α signal; (b) expanded trace for the light diode and microwave signals, with the time interval between the microwave signals giving a pellet velocity of 0.505 km/s; (c) expanded trace for the timing and D_α signals showing a pellet lifetime of 0.983 ms after passing R_{lim}, giving a penetration depth of $\lambda_{D_\alpha} = 0.49$ m.
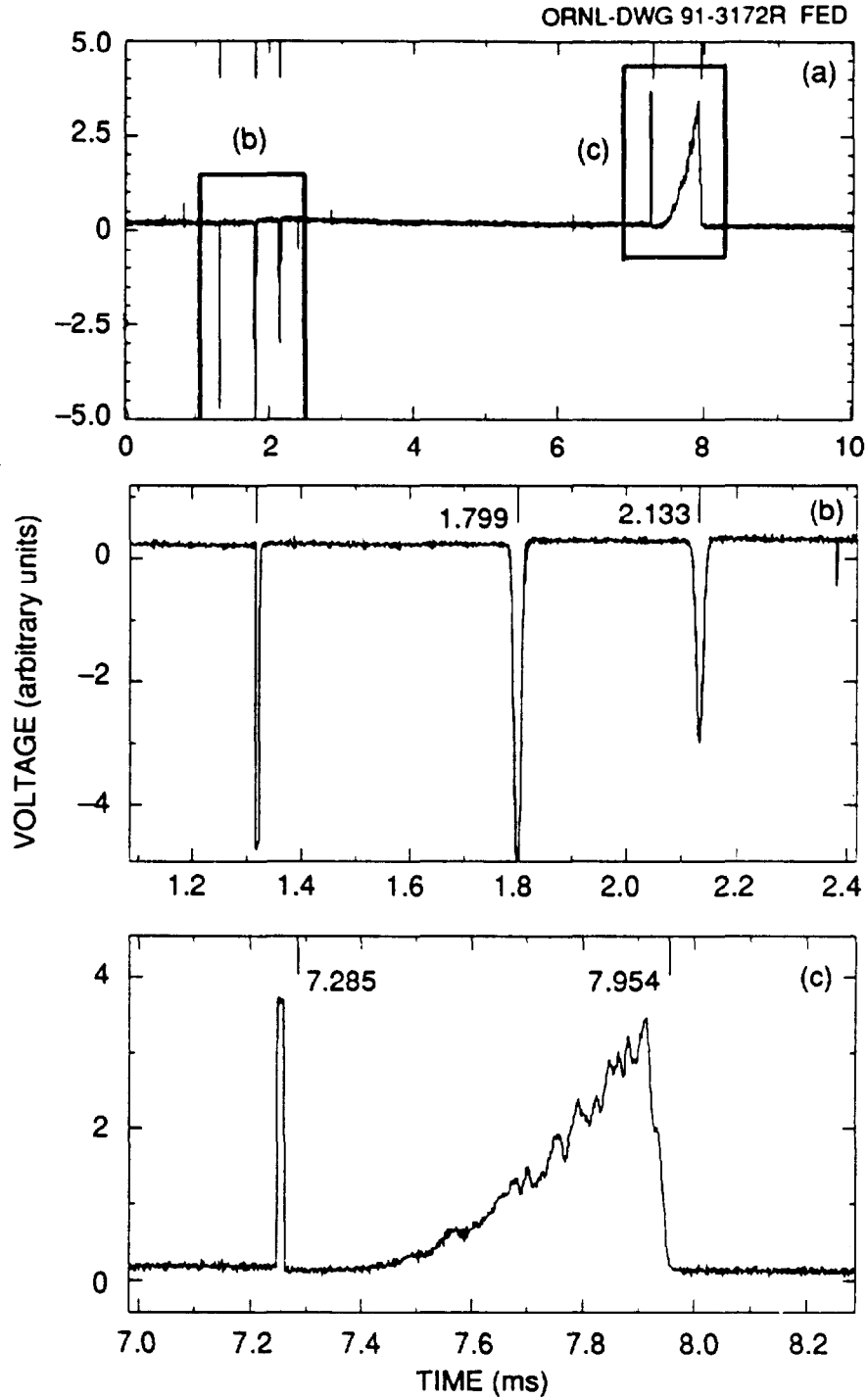
FIG. 2. Typical diagnostic trace (shot 20387, pellet 1) for normal velocity 4.0 mm pellets: (a) combined signals; (b) expanded trace for the light diode and microwave signals with the time interval between the microwave signals giving a pellet velocity of 1.245 km/s; (c) expanded trace for the timing and D_α signals showing a pellet lifetime of 0.669 ms, giving a penetration depth of $\lambda_{D_\alpha} = 0.83$ m.
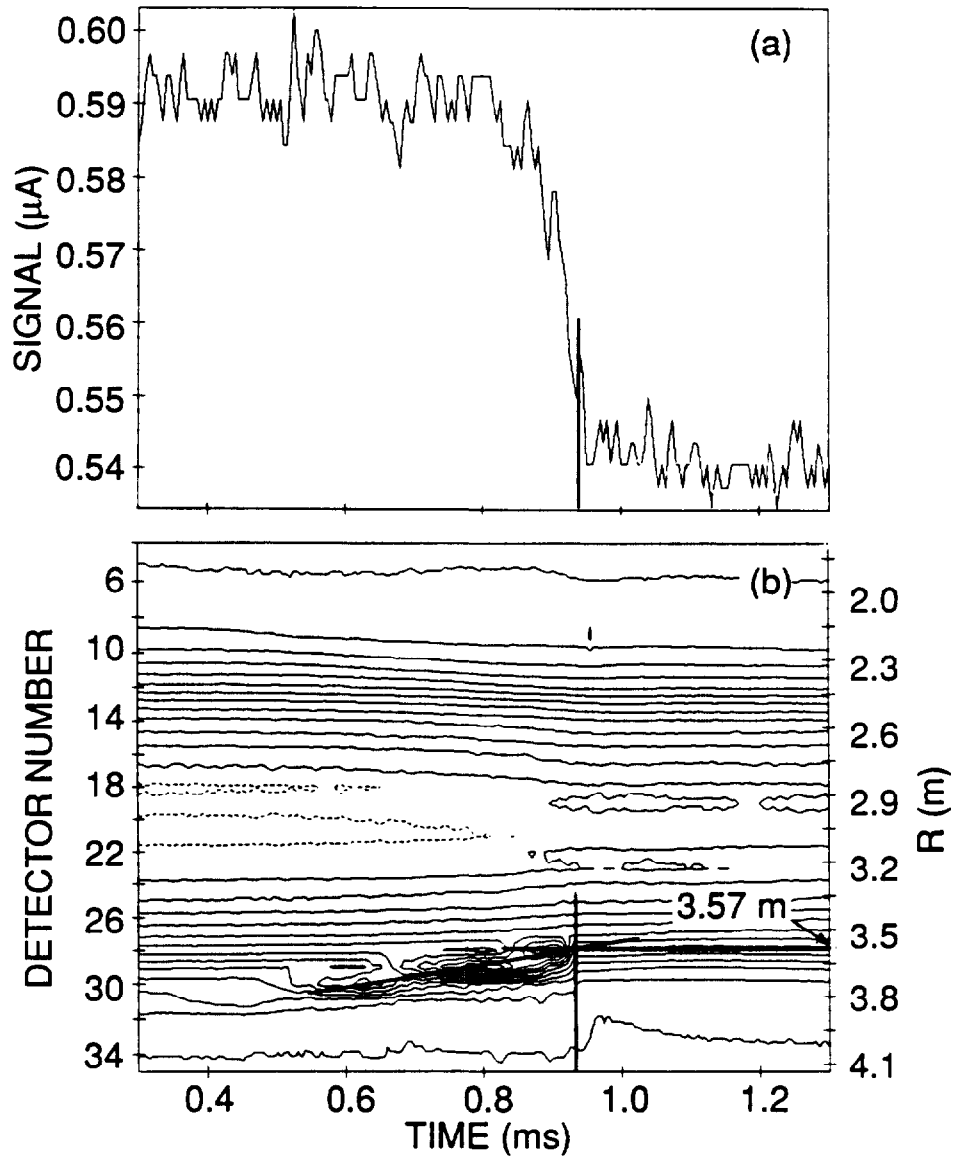
FIG. 3. Typical SXR traces (shot 20732, pellet 2) for determining the penetration depth of low velocity 2.7 mm pellets: (a) horizontal channel signal in the plasma midplane for determining the end of pellet ablation; (b) composite of the vertical channel signals indicating the uncorrected major radius of penetration at $R = 3.57$ m corrected to $R_{pen}^{SXR} = 3.635$ m, which corresponds to $\lambda_{SXR} = 0.50$ m.
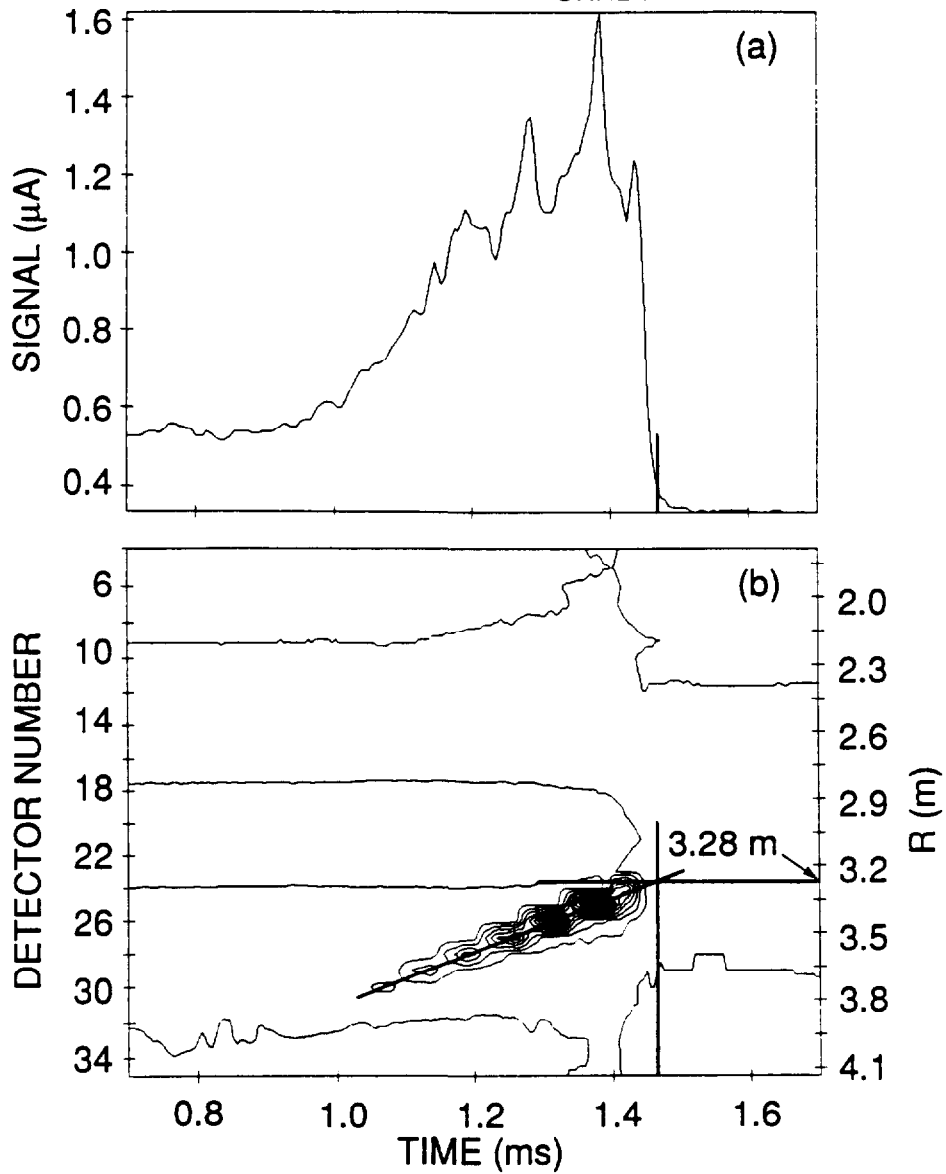
FIG. 4. Typical SXR traces (shot 20387, pellet 1) for determining the penetration depth of normal velocity 4.0 mm pellets: (a) horizontal channel in the plasma midplane for determining the end of pellet ablation; (b) composite of the vertical channel signals indicating the uncorrected major radius of penetration at $R = 3.28$ m corrected to $R_{pen}^{SXR} = 3.345$ m, which corresponds to $\lambda_{SXR} = 0.79$ m.
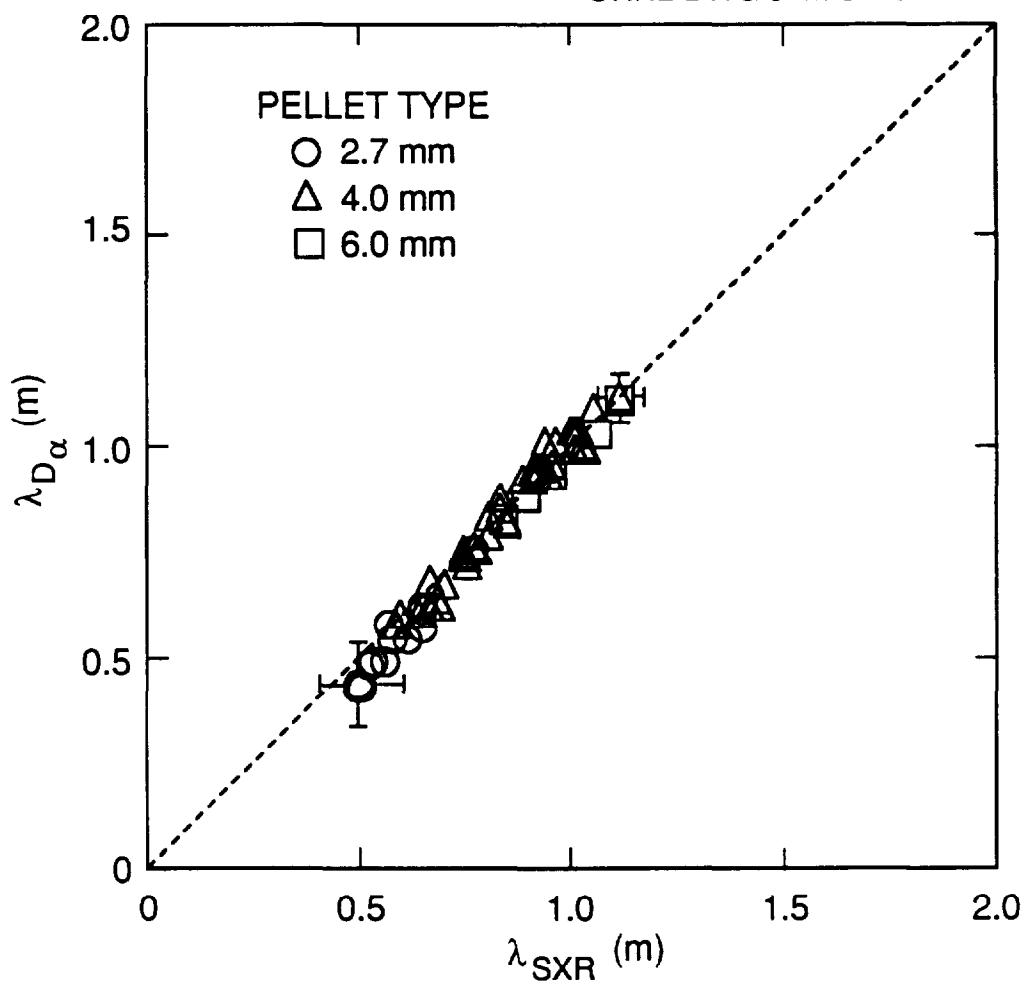
FIG. 5. The penetration depths from time-of-flight (λ_{D_α}) and SXR (λ_{SXR}) analyses agree well over the entire range of penetration. Error bars are estimated at ± 0.05 m for 4.0 and 6.0 mm pellets and ± 0.10 m for 2.7 mm pellets.
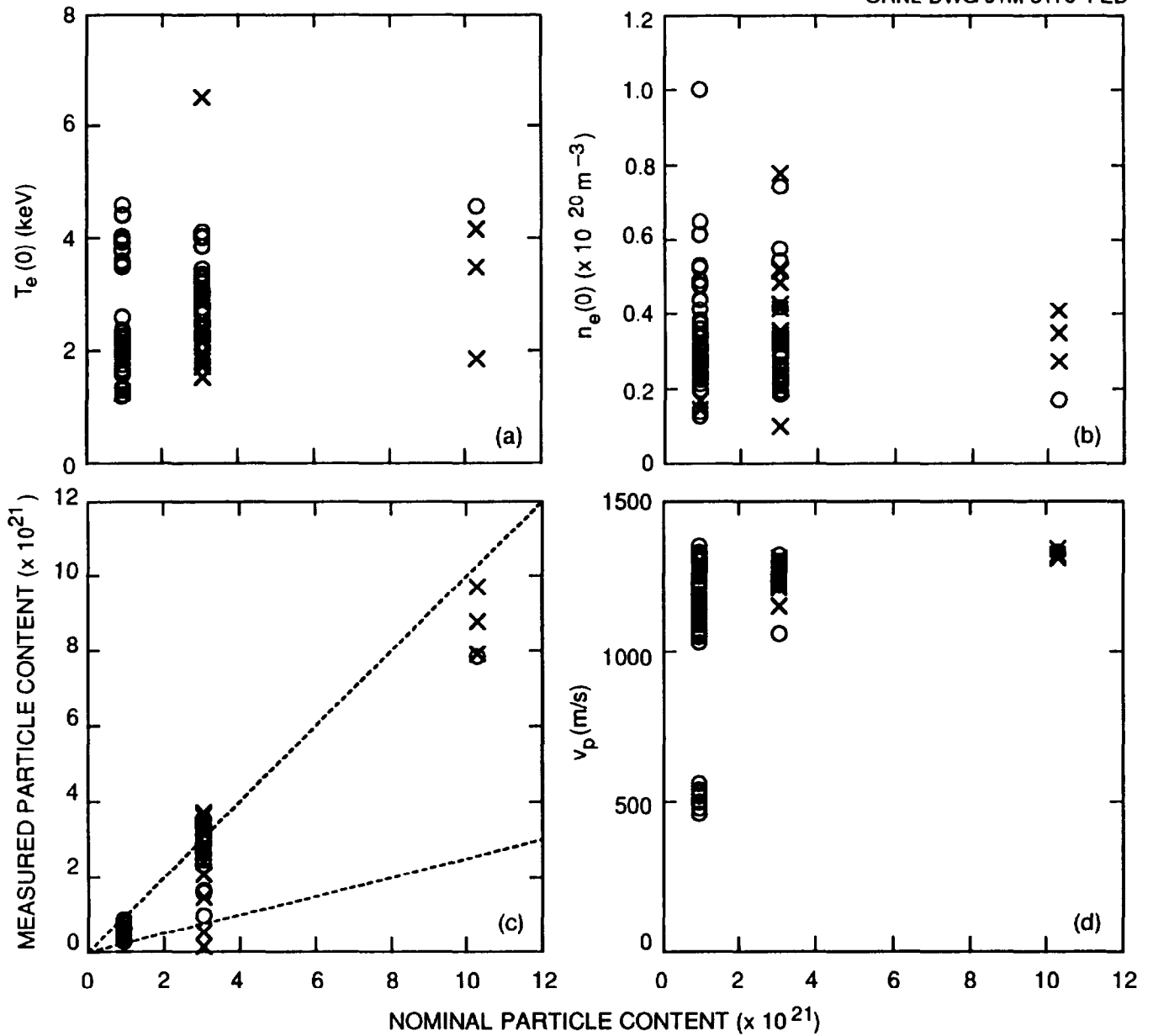
FIG. 6. Data ranges for each of the three pellet sizes, indicating those that did (o) and did not (×) meet selection criteria on minimum size and maximum penetration depth for the empirical fit to penetration: (a) central electron temperature; (b) central electron density; (c) pellet particle content (mass) showing curves of 100% and 25% (lower cutoff) of the nominal cylindrical pellet content; (d) pellet velocity.
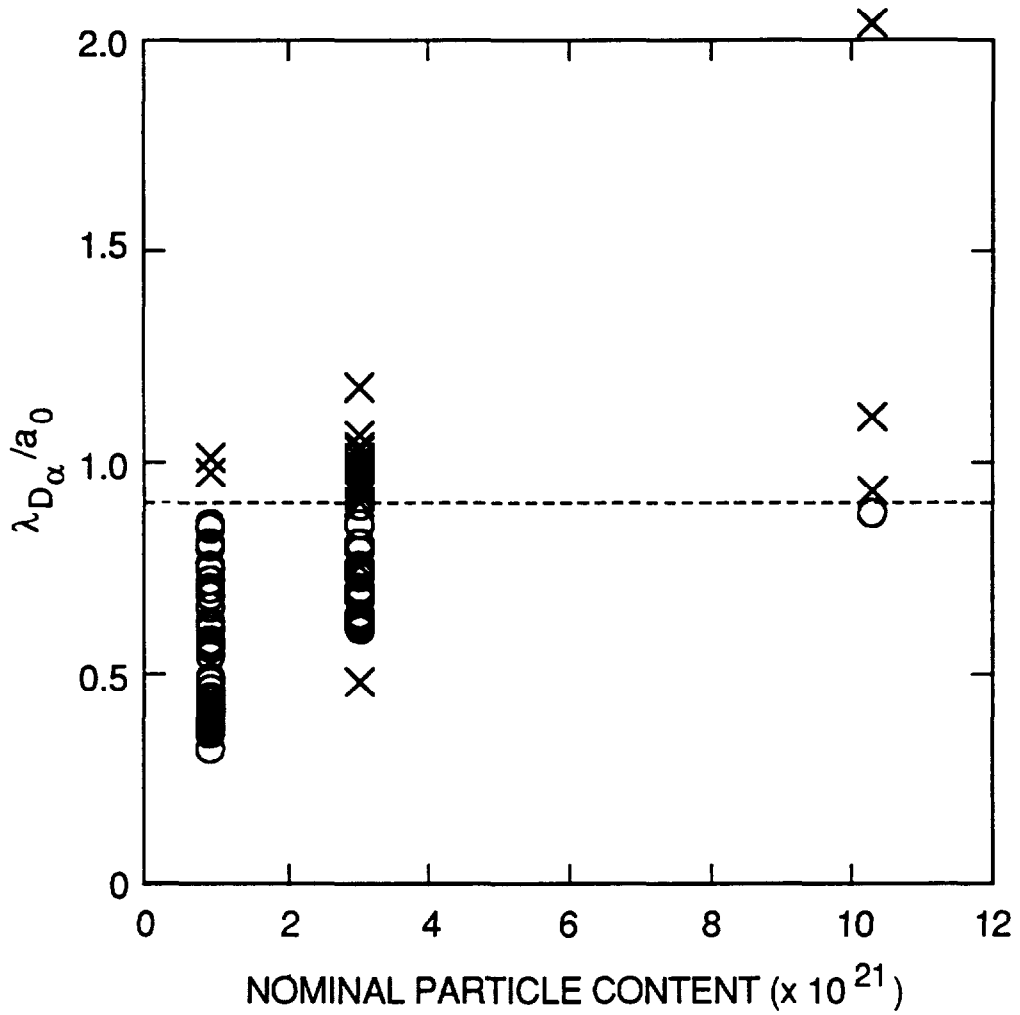
FIG. 7. Pellet penetration depths for each of the three pellet sizes, showing the cutoff at $\lambda/a_0 = 0.9$ for the empirical fit, indicating those that did (o) and did not (×) meet all selection criteria.
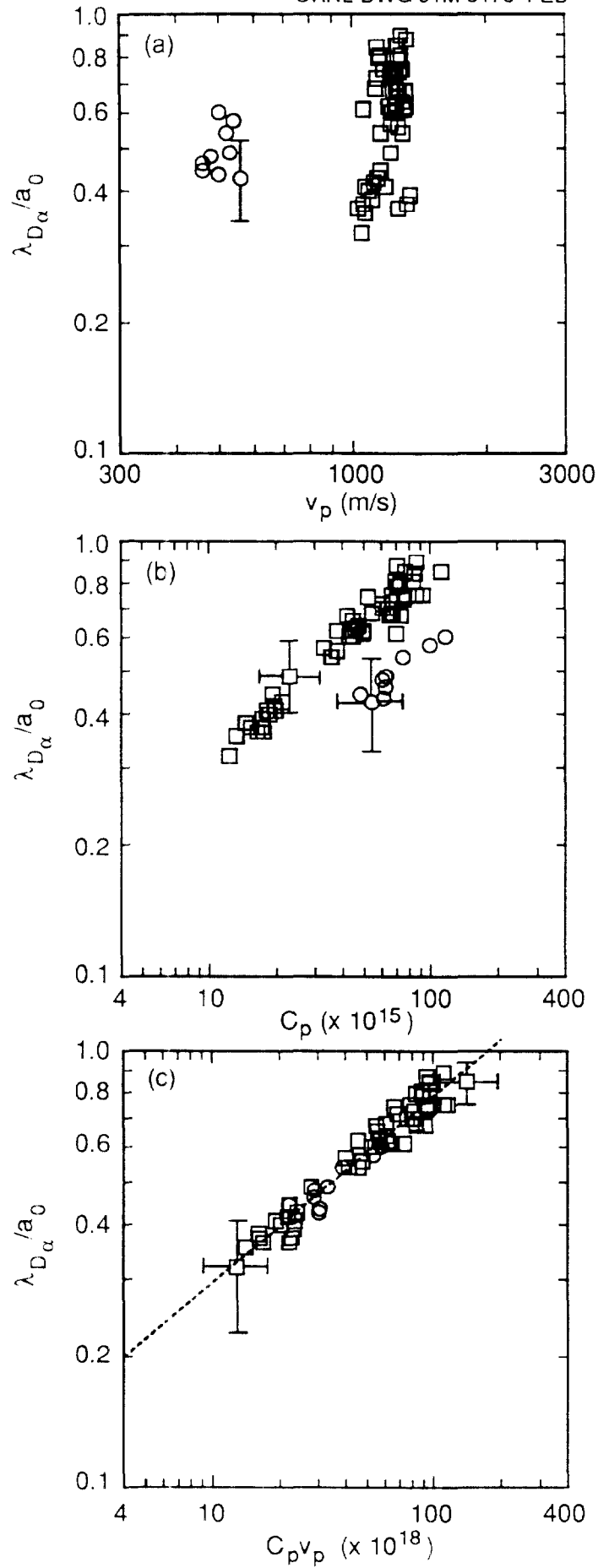
FIG. 8. Normalized pellet penetration depth (a) as a function of velocity; (b) as a function of C_p; (c) as a function of $C_p v_p$ derived from the NGS model showing a least-squares fit to the data. Circles denote the low velocity pellets and squares the nominal full velocity pellets.
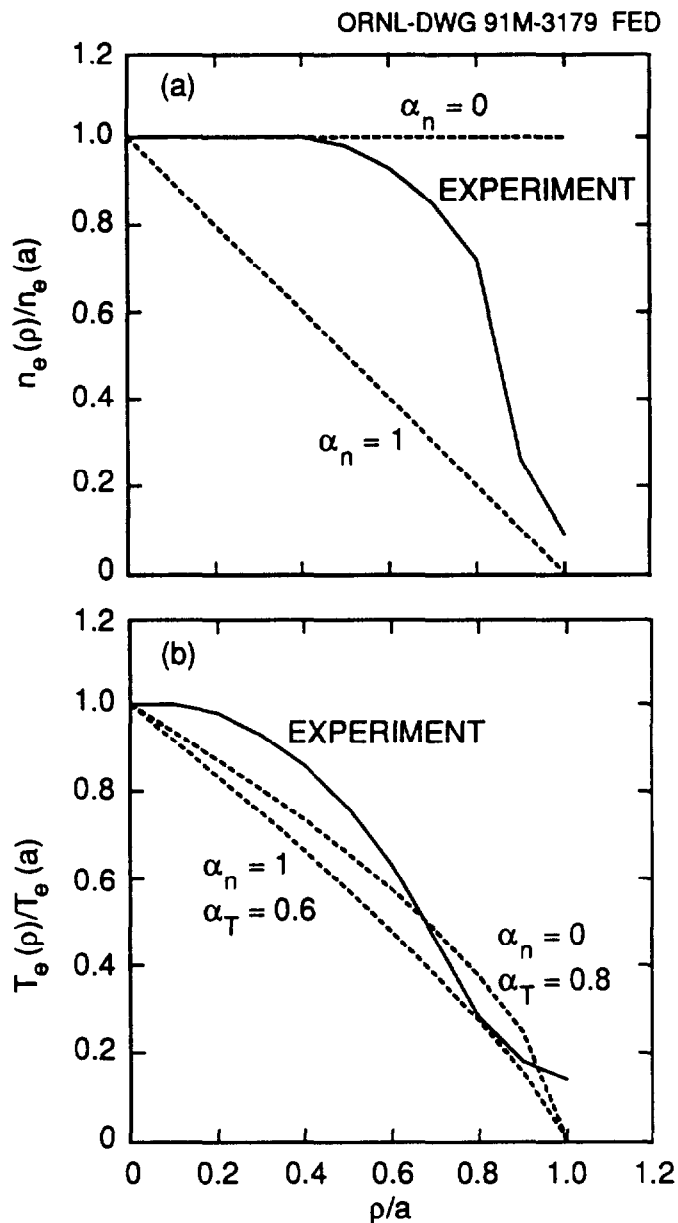
FIG. 9. Experimental profiles (shot 20732, just prior to pellet 1) and approximations to profiles of (a) electron density normalized to $n_e(0) = 2.3 \times 10^{19}$ m^{-3} and the flat ($\alpha_n = 0$) and linear profile approximations ($\alpha_n = 1$); (b) electron temperature normalized to $T_e(0) = 2.36$ keV and the profiles inferred from the empirical fit to pellet penetration [$\beta = 0.426 = 3/(3 + \alpha_n + 5\alpha_T)$] in the $\alpha_n = 0$ and $\alpha_n = 1$ limits.
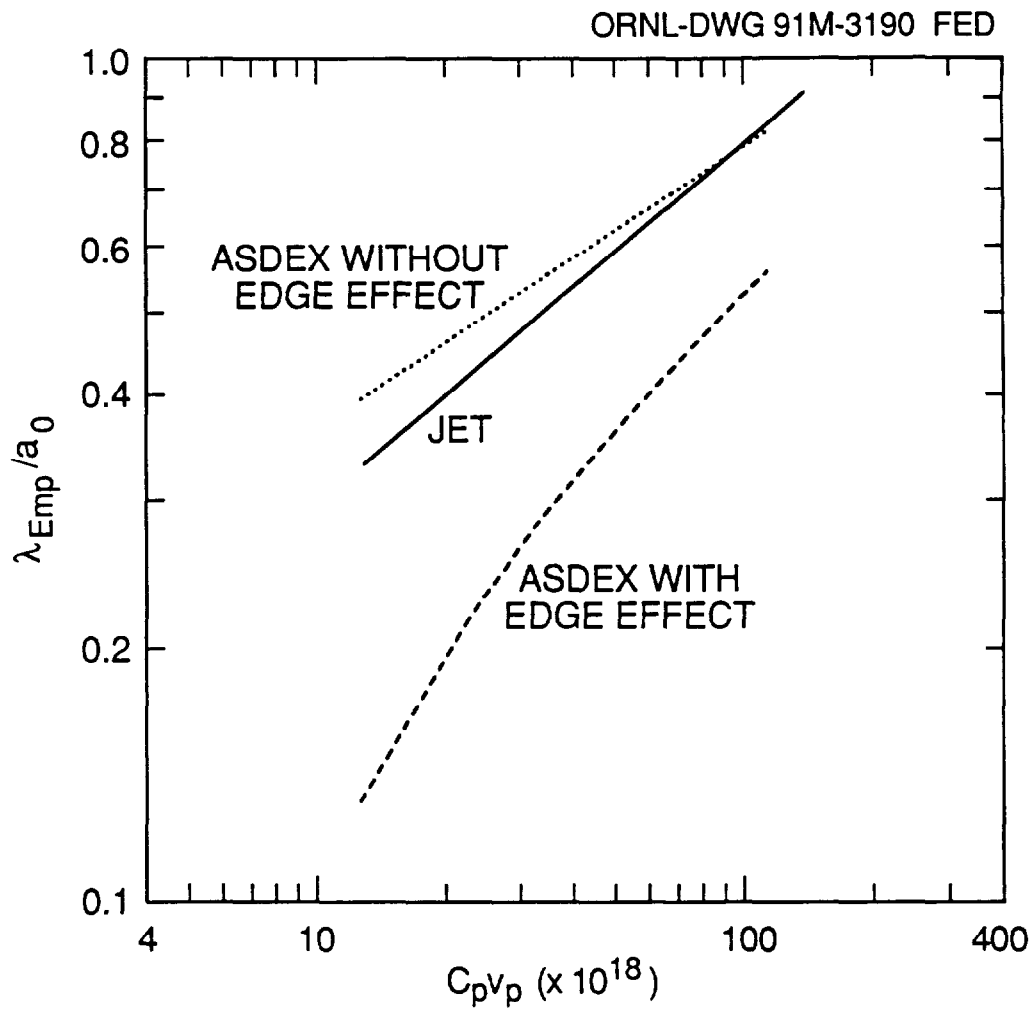
FIG. 10. The empirical fit to JET data shows the same scaling as the fit to ASDEX data by Büchl et al., but penetration is significantly deeper in JET. Neglecting the offset in the ASDEX fit brings the results into reasonable agreement.
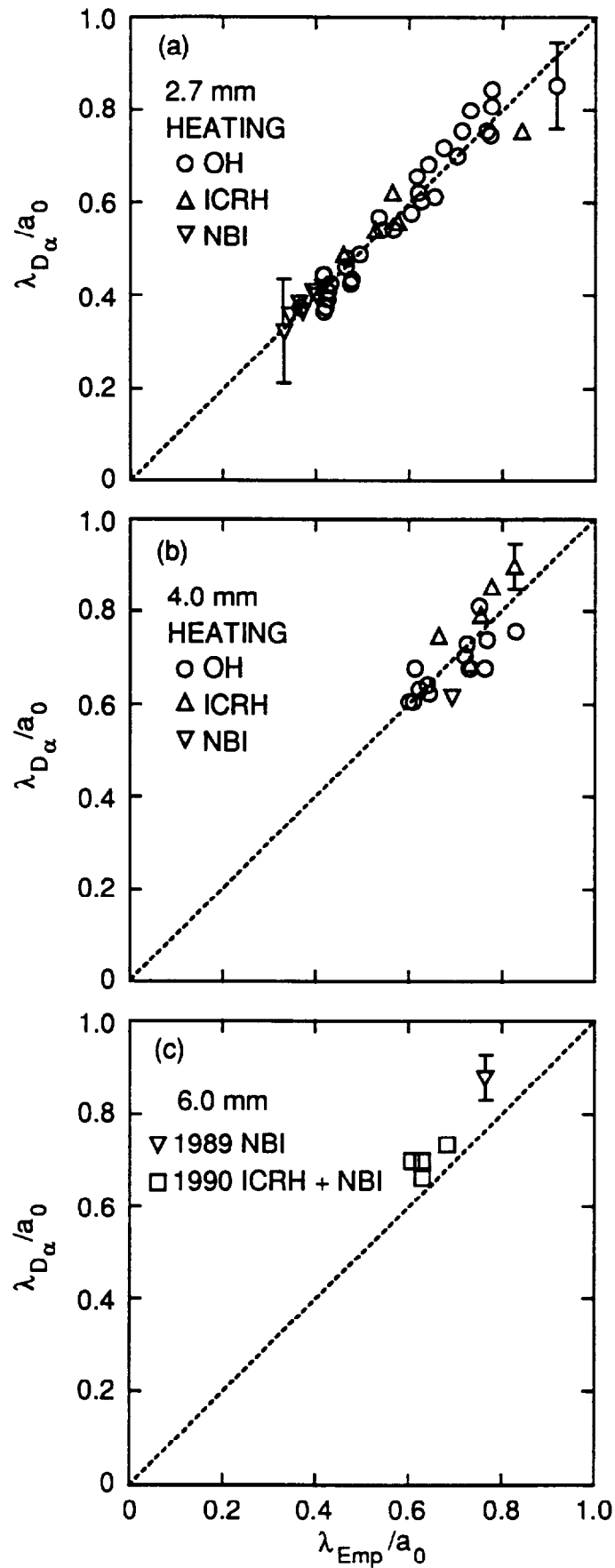
FIG. 11. The measured penetration compared with the empirical fit for (a) 2.7 mm pellets; (b) 4 mm pellets; (c) 6 mm pellets where the mass and velocity have been estimated for the 1990 data.
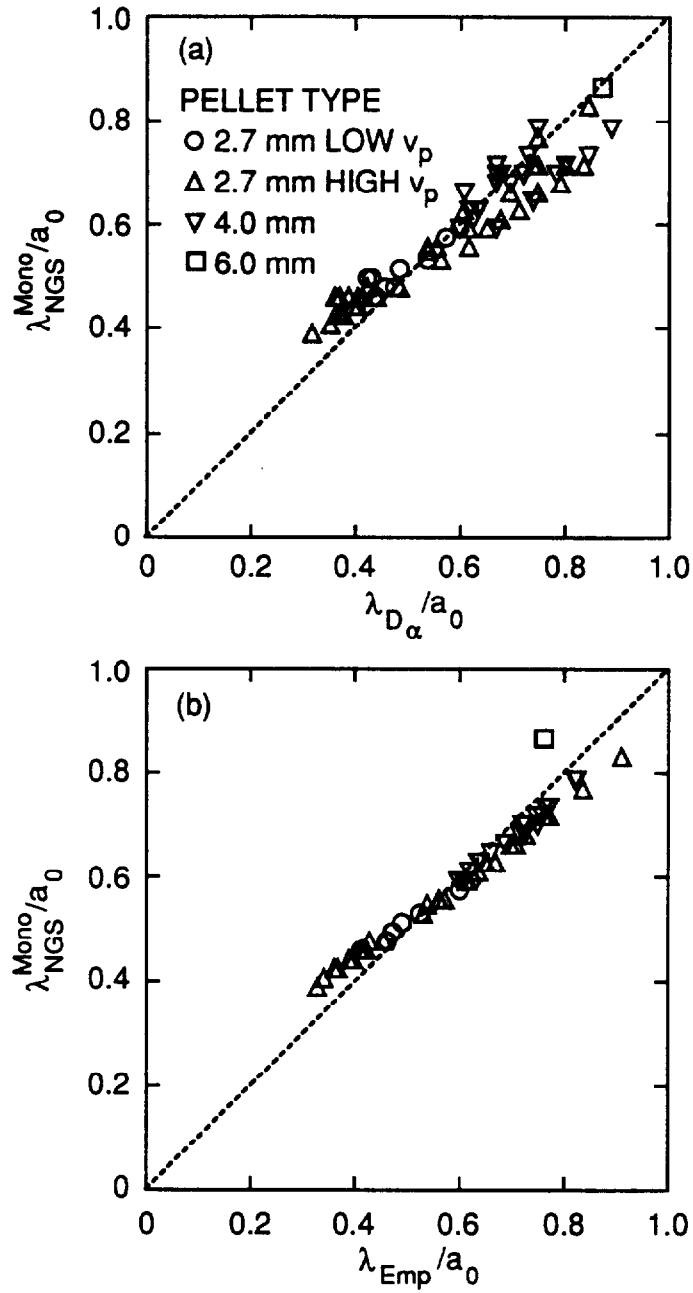
FIG. 12. The penetration depth calculated by PELLET with the monoenergetic electron NGS model compared with (a) the measured penetration depth and (b) the empirical fit to penetration depth. Agreement is good over the entire range of parameters.
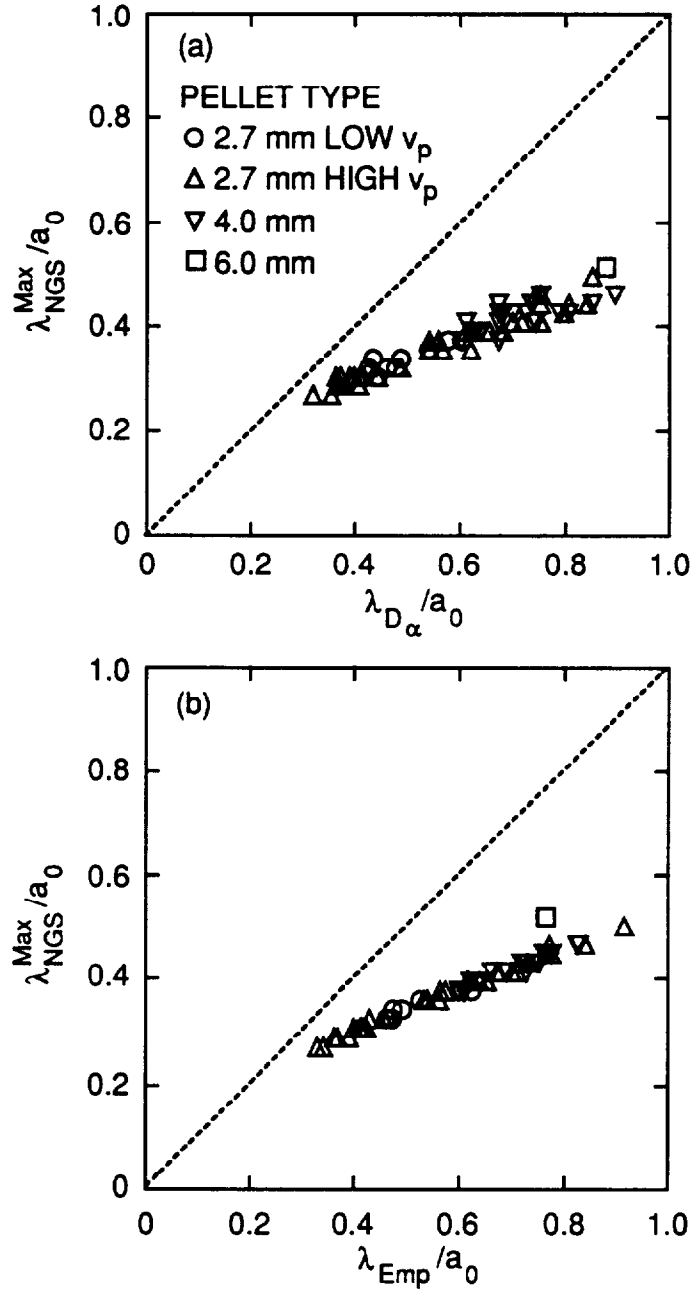
FIG. 13. The penetration depth calculated by PELLET with the Maxwellian electron NGS model compared with (a) the measured penetration depth and (b) the empirical fit to penetration depth. The Maxwellian approximation leads to higher ablation rates and lower penetration than observed experimentally.
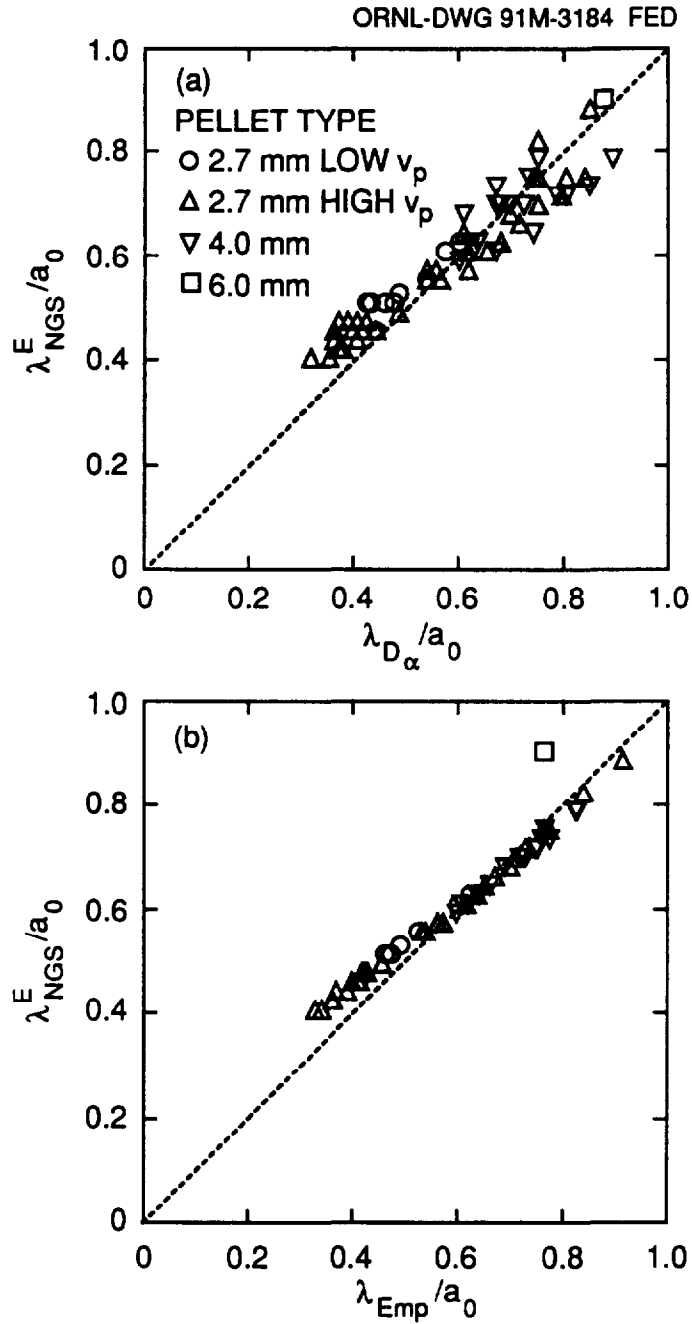
FIG. 14. Pellet penetration depth calculated by PELLET with the Maxwellian electron NGS model and a shield enhancement factor compared with (a) the measured penetration depth and (b) the empirical fit to penetration depth. The inclusion of a Maxwellian distribution of incident electrons requires a compensating enhancement of the shielding by a factor of ≈ 15 in order to reproduce the penetration data.
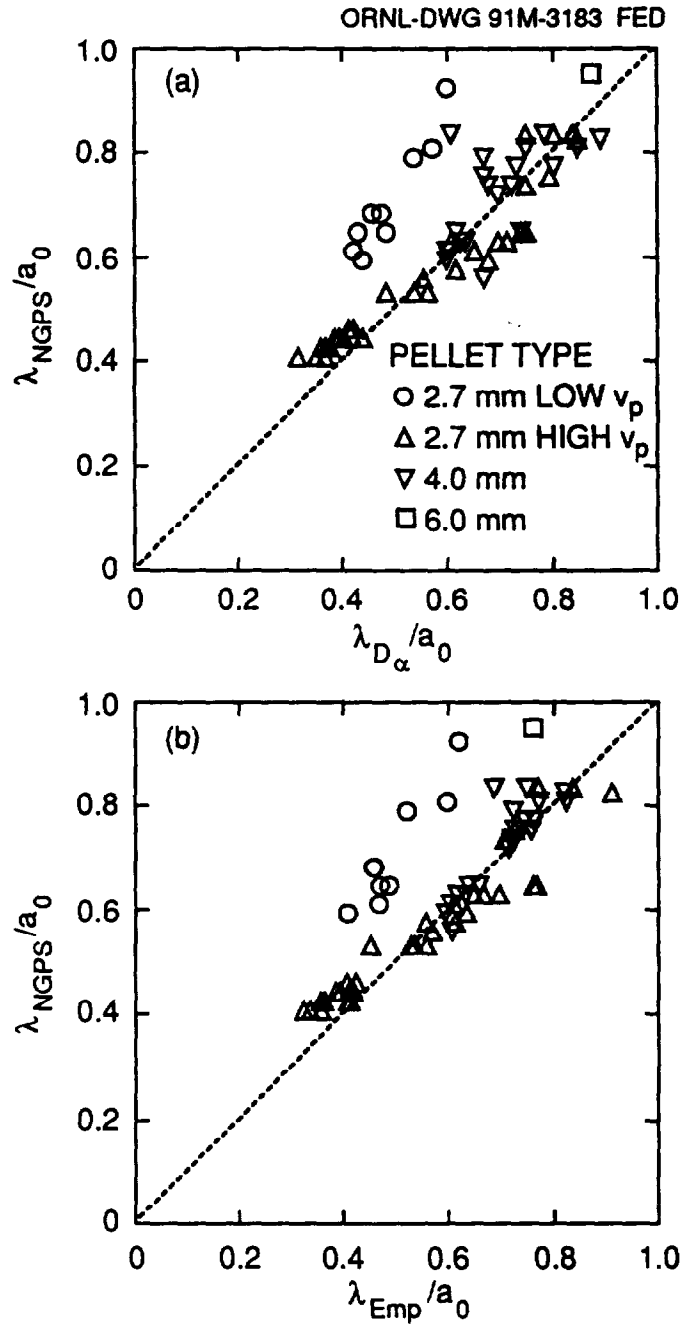
FIG. 15. The penetration depth calculated by PELLET with the Maxwellian electron NGPS model compared with (a) the measured penetration depth and (b) the empirical fit to penetration depth. The penetration of both low and normal velocity pellets cannot be reproduced by the same empirical choice of ionization radius (flux tube dimension), which yields weak to non-existent velocity scaling, contrary to the experimental data.

ANNEX

P.-H. REBUT, A. GIBSON, M. HUGUET, J.M. ADAMS[1], B. ALPER, H. ALTMANN, A. ANDERSEN[2], P. ANDREW[3],
M. ANGELONE[4], S. ALI-ARSHAD, P. BAIGGER, W. BAILEY, B. BALET, P. BARABASCHI, P. BARKER, R. BARNSLEY[5],
M. BARONIAN, D.V. BARTLETT, L. BAYLOR[6], A.C. BELL, G. BENALI, P. BERTOLDI, E. BERTOLINI, V. BHATNAGAR,
A.J. BICKLEY, D. BINDER, H. BINDSLEV[2], T. BONICELLI, S.J. BOOTH, G. BOSIA, M. BOTMAN, D. BOUCHER,
P. BOUCQUEY, P. BREGER, H. BRELEN, H. BRINKSCHULTE, D. BROOKS, A. BROWN, T. BROWN, M. BRUSATI,
S. BRYAN, J. BRZOZOWSKI[7], R. BUCHSE[22], T. BUDD, M. BURES, T. BUSINARO, P. BUTCHER, H. BUTTGEREIT,
C. CALDWELL-NICHOLS, D.J. CAMPBELL, P. CARD, G. CELENTANO, C.D. CHALLIS, A.V. CHANKIN[8], A. CHERUBINI,
D. CHIRON, J. CHRISTIANSEN, P. CHUILON, R. CLAESEN, S. CLEMENT, E. CLIPSHAM, J.P. COAD, I.H. COFFEY[9],
A. COLTON, M. COMISKEY[10], S. CONROY, M. COOKE, D. COOPER, S. COOPER, J.G. CORDEY, W. CORE, G. CORRIGAN,
S. CORTI, A.E. COSTLEY, G. COTTRELL, M. COX[11], P. CRIPWELL[12], O. Da COSTA, J. DAVIES, N. DAVIES, H. de BLANK,
H. de ESCH, L. de KOCK, E. DEKSNIS, F. DELVART, G.B. DENNE-HINNOV, G. DESCHAMPS, W.J. DICKSON[13], K.J. DIETZ,
S.L. DMITRENKO, M. DMITRIEVA[14], J. DOBBING, A. DOGLIO, N. DOLGETTA, S.E. DORLING. P.G. DOYLE, D.F. DÜCHS,
H. DUQUENOY, A. EDWARDS, J. EHRENBERG, A. EKEDAHL, T. ELEVANT[7], S.K. ERENTS[11], L.G. ERIKSSON,
H. FAJEMIROKUN[12], H. FALTER, J. FREILING[15], F. FREVILLE, C. FROGER, P. FROISSARD, K. FULLARD, M. GADEBERG,
A. GALETSAS, T. GALLAGHER, D. GAMBIER, M. GARRIBBA, P. GAZE, R. GIANNELLA, R.D. GILL, A GIRARD,
A. GONDHALEKAR, D. GOODALL[11], C. GORMEZANO, N.A. GOTTARDI, C. GOWERS, B.J. GREEN, B. GRIEVSON, R. HAANGE,
A. HAIGH, C.J. HANCOCK, P.J. HARBOUR, T. HARTRAMPF, N.C. HAWKES[11], P. HAYNES[11], J.L. HEMMERICH, T. HENDER[11],
J. HOEKZEMA, D. HOLLAND, M. HONE, L. HORTON, J. HOW, M. HUART, I. HUGHES, T.P. HUGHES[10], M. HUGON, Y. HUO[16],
K. IDA[17], B. INGRAM, M. IRVING, J. JACQUINOT, H. JAECKEL, J.F. JAEGER, G. JANESCHITZ, Z. JANKOVICZ[18], O.N. JARVIS,
F. JENSEN, E.M. JONES, H.D. JONES, L.P.D.F. JONES, S. JONES[19], T.T.C. JONES, J.-F. JUNGER, F. JUNIQUE, A. KAYE,
B.E. KEEN, M. KEILHACKER, G.J. KELLY, W. KERNER, A. KHUDOLEEV[21], R. KONIG, A. KONSTANTELLOS, M. KOVANEN[20],
G. KRAMER[15], P. KUPSCHUS, R. LÄSSER, J.R. LAST, B. LAUNDY, L. LAURO-TARONI, M. LAVEYRY, K. LAWSON[11],
M. LENNHOLM, J. LINGERTAT[22], R.N. LITUNOVSKI, A. LOARTE, R. LOBEL, P. LOMAS, M. LOUGHLIN, C. LOWRY, J. LUPO,
A.C. MAAS[15], J. MACHUZAK[19], B. MACKLIN, G. MADDISON[11], C.F. MAGGI[23], G. MAGYAR, W. MANDL[22], V. MARCHESE,
G. MARCON, F. MARCUS, J. MART, D. MARTIN, E. MARTIN, R. MARTIN-SOLIS[24], P. MASSMANN, G. MATTHEWS,
H. McBRYAN, G. McCRACKEN[11], J. McKIVITT, P. MERIGUET, P. MIELE, A. MILLER, J. MILLS, S.F. MILLS, P. MILLWARD,
P. MILVERTON, E. MINARDI[4], R. MOHANTI[25], P.L. MONDINO, D. MONTGOMERY[26], A. MONTVAI[27], P. MORGAN,
H. MORSI, D. MUIR, G. MURPHY, R. MYRNÄS[28], F. NAVE[29], G. NEWBERT, M. NEWMAN, P. NIELSEN, P. NOLL,
W. OBERT, D. O'BRIEN, J. ORCHARD, J. O'ROURKE, R. OSTROM, M. OTTAVIANI, M. PAIN, F. PAOLETTI,
S. PAPASTERGIOU, W. PARSONS, D. PASINI, D. PATEL, A. PEACOCK, N. PEACOCK[11], R.J.M. PEARCE, D. PEARSON[12],
J.F. PENG[16], R. PEPE DE SILVA, G. PERINIC, C. PERRY, M. PETROV[21], M.A. PICK, J. PLANCOULAINE, J.-P POFFÉ,
R. PÖHLCHEN, F. PORCELLI, L. PORTE[13], R. PRENTICE, S. PUPPIN, S. PUTVINSKII[8], G. RADFORD[30], T. RAIMONDI,
M.C. RAMOS DE ANDRADE, R. REICHLE, J. REID, S. RICHARDS, E. RIGHI, F. RIMINI, D. ROBINSON[11], A. ROLFE,
R.T. ROSS, L. ROSSI, R. RUSS, P. RUTTER, H.C. SACK, G. SADLER, G. SAIBENE, J.L. SALANAVE, G. SANAZZARO,
A. SANTAGIUSTINA, R. SARTORI, C. SBORCHIA, P. SCHILD, M. SCHMID, G. SCHMIDT[31], B. SCHUNKE, S.M. SCOTT,
L. SERIO, A SIBLEY, R. SIMONINI, A.C.C. SIPS, P. SMEULDERS, R. SMITH, R. STAGG, M. STAMP, P. STANGEBY[3],
R. STANKIEWICZ[32], D.F. START, C.A. STEED, D. STORK, P.E. STOTT, P. STUBBERFIELD, D. SUMMERS, H. SUMMERS[13],
L. SVENSSON, J.A. TAGLE[33], M. TALBOT, A. TANGA, A. TARONI, C. TERELLA, A TERRINGTON, A TESINI, P.R. THOMAS,
E. THOMPSON, K. THOMSEN, F. TIBONE, A. TISCORNIA, P. TREVALION, B. TUBBING, P. VAN BELLE, H. VAN DER BEKEN,
G. VLASES, M. VON HELLERMANN, T. WADE, C. WALKER, R. WALTON[31], D. WARD, M.L. WATKINS, N. WATKINS,
M.J. WATSON, S. WEBER[34], J. WESSON, T.J. WIJNANDS, J. WILKS, D. WILSON, T. WINKEL, R. WOLF, D. WONG,
C. WOODWARD, Y. WU[35], M. WYKES, D. YOUNG, I.D. YOUNG, L. ZANNELLI, A. ZOLFAGHARI[19], W. ZWINGMANN

18

[1] Harwell Laboratory, UKAEA, Harwell, Didcot, Oxfordshire, UK.
[2] Risø National Laboratory, Roskilde, Denmark.
[3] Institute for Aerospace Studies, University of Toronto, Downsview, Ontario, Canada.
[4] ENEA Frascati Energy Research Centre, Frascati, Rome, Italy.
[5] University of Leicester, Leicester, UK.
[6] Oak Ridge National Laboratory, Oak Ridge, TN, USA.
[7] Royal Institute of Technology, Stockholm, Sweden.
[8] I.V. Kurchatov Institute of Atomic Energy, Moscow, Russian Federation.
[9] Queens University, Belfast, UK.
[10] University of Essex, Colchester, UK.
[11] Culham Laboratory, UKAEA, Abingdon, Oxfordshire, UK.
[12] Imperial College of Science, Technology and Medicine, University of London, London, UK.
[13] University of Strathclyde, Glasgow, UK.
[14] Keldysh Institute of Applied Mathematics, Moscow, Russian Federation.
[15] FOM-Institute for Plasma Physics "Rijnhuizen", Nieuwegein, Netherlands.
[16] Institute of Plasma Physics, Academia Sinica, Hefei, Anhui Province, China.
[17] National Institute for Fusion Science, Nagoya, Japan.
[18] Soltan Institute for Nuclear Studies, Otwock/Świerk, Poland.
[19] Plasma Fusion Center, Massachusetts Institute of Technology, Boston, MA, USA.
[20] Nuclear Engineering Laboratory, Lappeenranta University, Finland.
[21] A.F. Ioffe Physico-Technical Institute, St. Petersburg, Russian Federation.
[22] Max-Planck-Institut für Plasmaphysik, Garching, Germany.
[23] Department of Physics, University of Milan, Milan, Italy.
[24] Universidad Complutense de Madrid, Madrid, Spain.
[25] North Carolina State University, Raleigh, NC, USA.
[26] Dartmouth College, Hanover, NH, USA.
[27] Central Research Institute for Physics, Budapest, Hungary.
[28] University of Lund, Lund, Sweden.
[29] Laboratorio Nacional de Engenharia e Tecnologia Industrial, Sacavem, Portugal.
[30] Institute of Mathematics, University of Oxford, Oxford, UK.
[31] Princeton Plasma Physics Laboratory, Princeton University, Princeton, NJ, USA.
[32] RCC Cyfronet, Otwock/Świerk, Poland,
[33] Centro de Investigaciones Energéticas, Medioambientales y Tecnológicas, Madrid, Spain.
[34] Freie Universität, Berlin, Germany.
[35] Insitute for Mechanics, Academia Sinica, Beijing, China.